In situ X-ray studies of adlayer-induced crystal nucleation at the liquid–liquid interface

Annika Elsen[a], Sven Festersen[a], Benjamin Runge[a], Christian T. Koops[a], Benjamin M. Ocko[b], Moshe Deutsch[c], Oliver H. Seeck[d], Bridget M. Murphy[a,e,1], and Olaf M. Magnussen[a,e]

[a]Institute for Experimental and Applied Physics, Christian-Albrechts-University Kiel, 24098 Kiel, Germany; [b]Condensed Matter Physics and Materials Science Department, Brookhaven National Laboratory, Upton, NY 11973; [c]Physics Department, and Institute of Nanotechnology and Advanced Materials, Bar-Ilan University, Ramat-Gan 52900, Israel; [d]Deutsches Elektronensynchrotron DESY, 22607 Hamburg, Germany; and [e]Ruprecht Haensel Laboratory, Christian-Albrechts-University Kiel, 24098 Kiel, Germany

Edited by David A. Weitz, Harvard University, Cambridge, MA, and approved March 8, 2013 (received for review January 30, 2013)

Crystal nucleation and growth at a liquid–liquid interface is studied on the atomic scale by in situ Å-resolution X-ray scattering methods for the case of liquid Hg and an electrochemical dilute electrolyte containing Pb^{2+}, F^-, and Br^- ions. In the regime negative of the Pb amalgamation potential $\Phi_{rp} = -0.70$ V, no change is observed from the surface-layered structure of pure Hg. Upon potential-induced release of Pb^{2+} from the Hg bulk at $\Phi > \Phi_{rp}$, the formation of an intriguing interface structure is observed, comprising a well-defined 7.6-Å–thick adlayer, decorated with structurally related 3D crystallites. Both are identified by their diffraction peaks as PbFBr, preferentially aligned with their $\vec{c}$ axis along the interface normal. X-ray reflectivity shows the adlayer to consist of a stack of five ionic layers, forming a single-unit-cell–thick crystalline PbFBr precursor film, which acts as a template for the subsequent quasiepitaxial 3D crystal growth. This growth behavior is assigned to the combined action of electrostatic and short-range chemical interactions.

electrochemistry | liquid metal

Liquid–liquid and liquid–gas interfaces provide exciting new possibilities for material synthesis (1, 2). Contrary to solid interfaces, which exhibit strain and stress, heterogeneities, and defects such as steps, which all strongly affect growth processes, fluid systems provide soft, defect- and stress-free interfaces. The high mobility of reagents, products, and deposited particles in liquid phases facilitates the growth process as well as the self-assembly of ordered particle arrays at the interface.

A large variety of materials has been prepared via deposition at liquid–liquid interfaces, such as metals (1), oxides (3, 4), chalcogenides (5, 6), polymers (7), plasmonic materials (2), and nanoparticle catalysts of ceria (3), Pd (8, 9), and Pt (10). As demonstrated by Carim et al., deposition at liquid–liquid interfaces even allows the synthesis of group IV semiconductors such as Ge from oxide materials via a simple one-step, room-temperature electrochemical process (11). Different methods for nanoparticle manufacturing, such as deposition by reduction of metal ions (12) or electrochemical deposition (11), are available at the liquid–liquid interface, allowing for particle modification and growth control via adjustment of concentration or interfacial potential.

Despite the absence of long-range order, liquid interfaces provide the possibility to control the crystallinity, shape, and orientation of deposits. Examples are the growth of single-crystalline CuO and CuS films (4), the surfactant-induced oriented growth of calcite crystals (13), and the formation of pyramidal PbS crystallites with defined, high surface area facets (5). These phenomena were rationalized by energetic effects, such as the interface energies, surface charges, and specific chemical interactions, as well as by the growth kinetics. However, detailed insight into the phase formation mechanisms is generally precluded by lack of atomic-scale data on the interfacial processes, specifically on the initial stages of the crystal growth.

In contrast to solid surfaces and interfaces, structural studies of fluid interfaces, in particular of liquid–liquid interfaces, are experimentally very challenging. The consequent scarcity of such studies strongly inhibits progress in understanding and optimizing growth processes at these phase boundaries. For this reason, most studies have relied on ex situ structural characterization of the deposited structures, e.g., by electron microscopy or X-ray diffraction, after their transfer from the liquid to a solid substrate, which may substantially alter the deposit's structure and morphology (1). In situ structural investigations of growth at liquid–liquid interfaces, which would allow direct determination of the nanoscale deposit structure as well as monitoring its temporal evolution during the deposition process, have only been performed in a few rare cases for nanoparticle growth (14, 15) and were limited to nanometer resolution. Atomic-scale data on the structure of such interfaces have only been obtained in two Å-resolution X-ray studies of the Hg–electrolyte interface (16, 17) and were focused on the atomic layering in the Hg near-surface region as a function of potential and ion concentration.

Here, we describe an atomic-resolution study of the initial stages of crystal growth at a liquid–liquid interface, also using a Hg–electrolyte interface as a model system. We use a NaF base electrolyte containing strongly specifically adsorbing ions (Pb^{2+} and Br^-) and control the phase formation reaction electrochemically via a Faradaic reaction. Low ($\leq$10 mM) ion concentrations were used to avoid the adverse impurity effects plaguing interfacial electrochemical processes at higher ($\sim$1 M) concentrations. Macroscopic data on Hg in Pb^{2+}- and Br^--containing electrolytes, obtained in previous electrochemical studies, suggest high surface excess concentrations of these species, from which the presence of a close-packed, vertically ordered stack of $PbBr_2$ layer at the interface was argued (18, 19). However, rather than merely verifying these predictions our experiments revealed much more complex phenomena, specifically the formation of an ultrathin precursor layer that acts as a template for subsequent growth of highly aligned 3D crystalline deposits—a behavior which may help rationalize the previous indirect observations for quasiepitaxial growth at liquid–liquid interfaces.

Results

The cyclic voltammogram obtained for the interface of liquid Hg in 0.01 M NaF + 0.01 M NaBr + 0.25 mM $PbBr_2$ solution (*Materials and Methods*) is shown in Fig. 1*B*. It exhibits

Author contributions: B.M.O., M.D., B.M.M., and O.M.M. designed research; A.E., S.F., B.R., C.T.K., B.M.O., M.D., O.H.S., B.M.M., and O.M.M. performed research; B.R., C.T.K., O.H.S., and B.M.M. contributed new reagents/analytic tools; A.E., S.F., and B.M.M. analyzed data; and A.E., B.M.O., M.D., B.M.M., and O.M.M. wrote the paper.

The authors declare no conflict of interest.

This article is a PNAS Direct Submission.

[1]To whom correspondence should be addressed. E-mail: murphy@physik.uni-kiel.de.

This article contains supporting information online at www.pnas.org/lookup/suppl/doi:10.1073/pnas.1301800110/-/DCSupplemental.

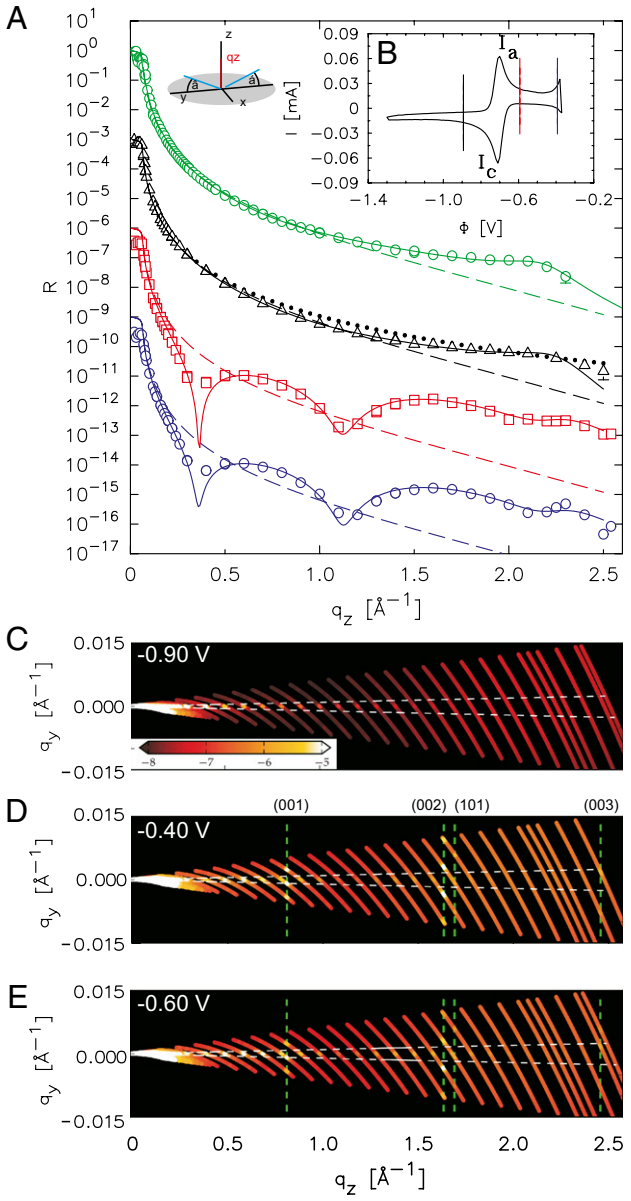

Fig. 1. Reflectivity curves (*A*) and full intensity maps in the q_y, q_z plane (*C–E*) at different potentials Φ for liquid Hg in 0.01 M NaF + 0.01 M NaBr + 0.25 mM $PbBr_2$ solution. (*A*) Measured XRR curves at −0.90 V (black triangles), −0.60 V (red squares), and −0.40 V (blue circles). For clarity, the XRR curves are offset by a factor of 10^{-3}. For comparison an XRR curve measured at the Hg–0.01 M NaF interface at −0.90 V is shown (green circles). Solid lines correspond to the best fits by the models described in the text, the dotted line to R_F, and the dashed lines to the reflectivity of an interface with a monotonic electron density profile with a Gaussian roughness of $\sigma = 1.00$ Å. (*B*) Corresponding cyclic voltammogram (scan rate 5 mV/s), with vertical lines marking the potentials of the XRR measurements. (*C–E*) Intensity maps in the q_y, q_z plane measured at (*C*) −0.90 V, (*D*) −0.40 V, and (*E*) −0.6 V. Each solid line corresponds to a 1D detector frame at a specific angle where the center of each line corresponds to $\alpha = \beta$ and where the color indicates the scattered intensity in logarithmic units. Horizontal white dashed lines indicate the angular range used in determining the reflectivity curves in *A* and vertical dashed lines mark the q_z positions of the 3D crystallites' diffraction spots.

a characteristic pair of redox peaks at $\Phi_{rp} \approx -0.70$ V, due to the Pb amalgamation reaction $Pb^{2+} + 2e^- \leftrightharpoons Pb^0(Hg)$. At $\Phi < \Phi_{rp}$ Pb amalgamates into Hg, depleting the electrolyte's interface of Pb^{2+} ions. At $\Phi > \Phi_{rp}$, the amalgamated $Pb^0(Hg)$ is released again as Pb^{2+} from the Hg electrode into the electrolyte's interface region.

To determine possible Φ-dependent variations in the structure of the Hg–electrolyte interface, we used X-ray reflectivity (XRR) measurements from the interface, $R(q_z)$, as a function of the incidence and exit angle $\alpha = \beta$ of the X-rays onto the interface (Fig. 1*A*, *Inset*) (20–22). Here, $q_z = (4\pi/\lambda)\sin\alpha$, $q_y = q_x = 0$ Å^{-1}, and λ is the X-rays' wavelength. The interface's structural information resides in the deviations of $R(q_z)$ from the theoretical Fresnel XRR curve of an ideally flat and abrupt interface. The roughness modified $R_F(q_z)$ is shown in dashed lines in Fig. 1*A*.

We used a 1D multipixel detector for our measurements. The detector's real-space straight line of pixels transforms into a curved trajectory in the $q_y - q_z$ plane. These trajectories are shown for each incidence angle in Fig. 1 *C–E* for different potentials. The reflectivity $R(q_z)$ is then determined by integrating the specularly reflected intensity over the angular resolution $\Delta\beta = 4.18$ mrad of the experiment, which corresponds to $\Delta q_y \approx 2.1 \times 10^{-3} q_z$ (marked by the white dashed lines in Fig. 1 *C–E*), and subtracting the background intensity measured at the off-specular condition of $\Delta q_x = \pm 0.015$ Å^{-1}. (For further details on the data processing, see Fig. S1).

From a large body of data, measured at the PETRA III synchrotron source at Deutsches Elektronensynchrotron (DESY) and the Advanced Photon Source (APS) Argonne National Laboratory, we show in Fig. 1*A* four typical $R(q_z)$ curves. At $\Phi = -0.90\,\text{V} < \Phi_{rp}$, the measured $R(q_z)$ (black triangles) is virtually identical with $R(q_z)$ observed for the neat Hg–0.01 M NaF interface at this potential (green circles) (16). Both curves exhibit the characteristic quasi-Bragg peak at $q_z = 2.25$ Å^{-1}, due to a depth-decaying Hg atomic layering at the interface, as well as the shallow dip in $R(q_z)$ below $R_F(q_z)$ (dotted line) at $0.5\,\text{Å}^{-1} \lesssim q_z \lesssim 1\,\text{Å}^{-1}$, due to a single suprainterface incomplete Hg atomic layer (16, 23). Thus, at $\Phi < \Phi_{rp}$ the interface structure is identical with that obtained for a dilute electrolyte containing nonspecifically adsorbing species only. This conclusion is supported by the detailed modeling of the interface-normal electron density profile, discussed below.

At $\Phi > \Phi_{rp}$, drastic changes are observed in the measured XRR curves. Although the quasi-Bragg peak, and hence the Hg layering, still persists, pronounced modulations appear in $R(q_z)$ (Fig. 1*A*, red squares and blue circles), indicating significant structural changes at the interface. Previous studies (22, 24, 25) identify such modulations as originating in a well-defined interfacial adlayer, having an electron density different from those of the two phases defining the interface. The modulations' period $\Delta q_z \approx 0.8$ Å^{-1} yields an estimated adlayer thickness of $d_{es} = 2\pi/\Delta q_z \approx 7.8$ Å. $R(q_z)$ at the modulations' maxima ($q_z \approx 0.8$ and 1.6 Å^{-1}) exceeds that measured at these q_z positions for $\Phi = -0.90$ V by more than 1 order of magnitude, indicating that the adlayer's electron density significantly exceeds that of the electrolyte. Moreover, the amplitude of the second maximum is even higher than that of the first, suggesting that the adlayer has a substructure consisting of several atomic layers (26). These conclusions are, again, supported by the detailed modeling below.

To obtain a detailed description of the laterally averaged surface-normal electron density profile $\rho_e(z)$, a physically motivated mathematical model for $\rho_e(z)$ is constructed. The squared modulus of the Fourier transform of the gradient of this model density is then fitted to the measured $R(q_z)$, yielding best-fit values for the parameters defining $\rho_e(z)$ (22, 27). For the smooth, nonmodulated $R(q_z)$ observed at $\Phi < \Phi_{rp}$ (Fig. 1*A*, black triangles) we used the distorted crystal (DC) model, previously used for Hg at the vapor (23, 28) and liquid interfaces (16, 17). This model mimics the decaying near-surface atomic layering of Hg by the sum of n equally spaced (d) Gaussians, the width of which is $\sigma = \sqrt{n\bar{\sigma}^2 + \sigma_T^2}$. The progressively larger widths with increasing depth (nd) increase the Gaussians' overlap, diminishing the amplitudes of the oscillations in their sum, and leading eventually to a roughly constant $\rho_e(z)$ at some depth below the

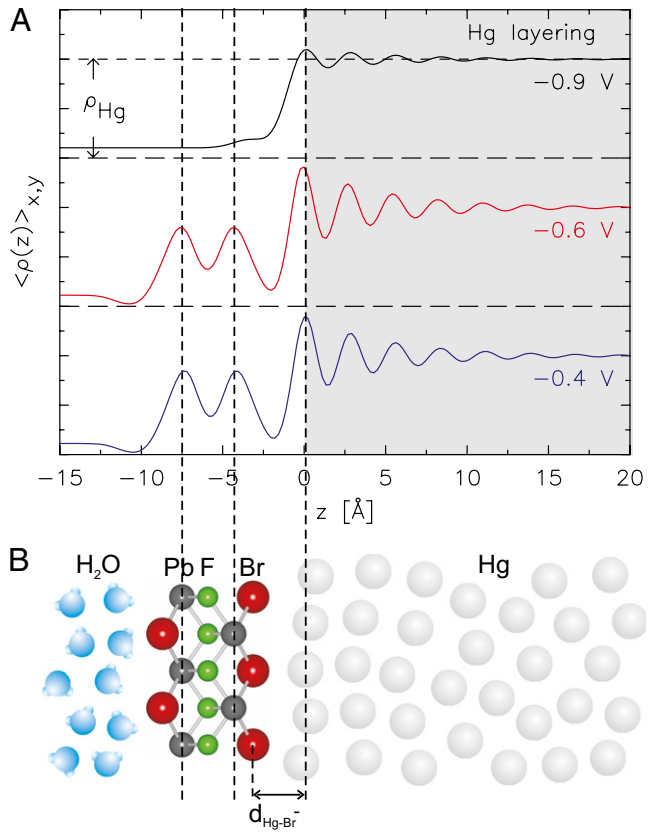

Fig. 2. (*A*) Electron density profiles for different potentials, corresponding to the best fits to the XRR data shown in Fig. 1*A*. (*B*) Schematic structural model of the PbFBr adlayer. Dashed lines indicate the positions of the two sheets of Pb ions and the topmost Hg layer.

interface. $\overline{\sigma}$ controls the decay length of the layering, and σ_T is a potential-dependent interfacial roughness, mainly due to thermal capillary waves (CWs), decorating all liquid interfaces (16, 29, 30). The electrolyte's electron density contribution is described by an error function which decreases monotonically at the interface. The previously detected (16, 17, 23) suprainterface partial Hg monolayer is represented by an additional Gaussian.

As shown by the black solid line in Fig. 1*A*, this model yields an excellent fit to the XRR curve measured at $\Phi = -0.90$ V. The corresponding electron density profile, shown in Fig. 2*A*, exhibits the features inferred above from the $R(q_z)$'s shape: the Hg layering and the suprainterface partial-density layer. The fit-obtained $d = 2.74 \pm 0.05$ Å, $\overline{\sigma} = 0.44 \pm 0.05$ Å, and $\sigma_T = 1.03 \pm 0.02$ Å coincide, within their error bars, with the corresponding values obtained for the Hg–0.01 M NaF interface (16). We conclude, therefore, that the amalgamation of Pb atoms into the Hg electrode does not seem to affect the interface structure. However, because the electron densities and radii of the Hg and Pb atoms are very similar, the presence of Pb atoms near the interface cannot be excluded.

The modulated, more complex $R(q_z)$ measured at $\Phi > \Phi_{rp}$ clearly requires a modification of the simple DC model used above. Fortunately, additional insight on the nature of the modulation-causing adlayer emerges from sharp diffraction peaks that are measured simultaneously with $R(q_z)$. The detector records the full intensity distribution along a varying-length arc in the (q_y, q_z) plane at each point of the reflectivity. Such arcs are shown in Fig. 1 *C*–*E*. For $\Phi < \Phi_{rp}$ (Fig. 1*C*) each arc exhibits only a single bright spot at $(q_y = 0,\ q_z > 0)$, formed by the specularly reflected beam. However, for $\Phi > \Phi_{rp}$ (Fig. 1 *D* and *E*) additional spots are observed (marked by green vertical dashed lines). These sharp, intense diffraction peaks occurring at $\Phi \geq -0.6$ V imply the presence of 3D crystallites at the interface in addition to the adlayer. This is clarified in Fig. 3*A*, which shows the intensity for $\Phi = -0.6$ V along the specular axis integrated over $\Delta q_y = \pm 0.003$ Å^{-1} without subtraction of the background intensity. In addition, the grazing incidence diffraction intensity spectrum at this potential is shown, which was obtained by scanning the 1D detector along the q_x direction and integrating the intensity over the q_z region of $0 - 0.3$ Å^{-1}.

The positions of the peaks observed by XRR in the (q_y, q_z) plane, and by grazing incidence diffraction measurements in the (q_x, q_z) plane, were compared with the 3D crystalline peak positions of 20 compounds (31–33), chemically possible in our system, shown in Fig. 3*A*. Only a single compound matches all observed peak positions: PbFBr. PbFBr has a layered tetragonal structure with lattice parameters $a = b = 4.18$ Å and $c = 7.59$ Å (Fig. 3 *B* and *C*) (34). Within its unit cell five layers of uniform atomic composition are stacked along the $\vec{c}$ axis. (In Fig. 3*B* the crystal arrangement is shown in the same orientation as in Fig. 2*B*.)

All (00ℓ) crystallite reflections lie around the q_z axis and can be described by Gaussian distributions with a FWHM of $0.102° \pm 0.003°$ indicating that the crystallites are preferentially oriented

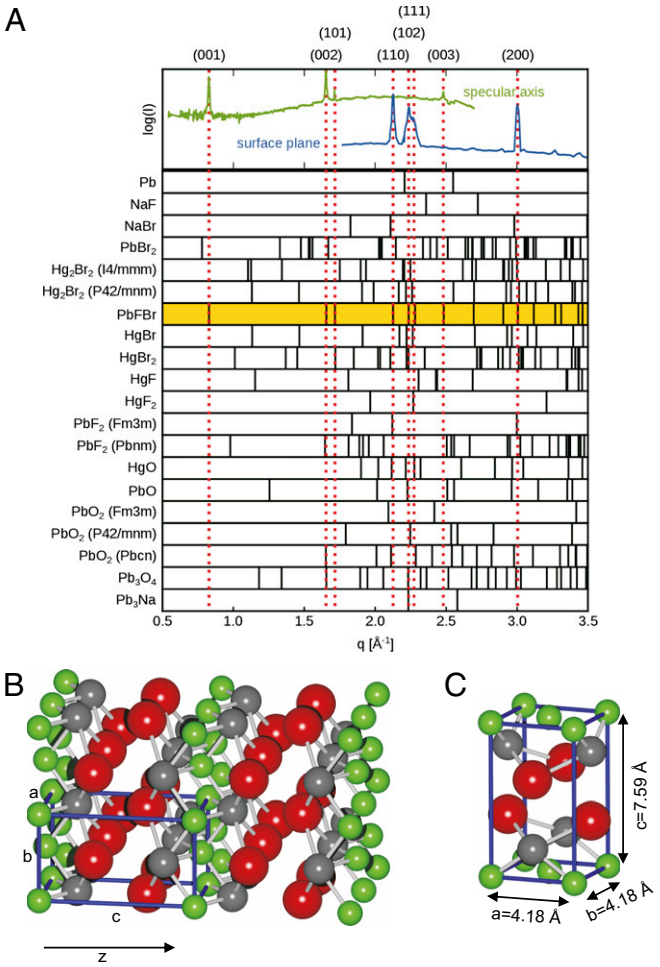

Fig. 3. (*A*) Comparison of the measured diffraction peaks (*Upper*) around the specular axis (green line) and near the surface plane (blue line) for $\Phi = -0.6$ V, with peak positions of 3D crystals of the compounds listed (*Lower*). The 3D crystallites' diffraction peak positions observed here are marked by red vertical dashed lines. $q = (q_x^2 + q_y^2 + q_z^2)^{1/2}$ is the total wave-vector transfer. (*B*) Crystal structure of PbFBr. Unit cell is marked in blue solid lines. The surface-normal direction *z* is also shown. (*C*) Unit cell of PbFBr.

with their c axis almost parallel to the Hg surface normal (Fig. S1). Based on this preferred orientation, and the c-lattice spacing's agreement with the estimated adlayer thickness d_{es}, the DC model used above was modified to represent the adlayer by a single-unit-cell–thick PbFBr layer, with the $\vec{c}$ axis pointing along q_z (Fig. 2*A*). This modeling is also supported by the high intensity of the high-q_z maximum ($q_z \approx 1.6$ Å^{-1}), indicating a substructure of several atomic layers within the adlayer. The five layers of ions within the PbFBr unit cell are described by Gaussians, convoluted each with the Fourier-transformed form factor of the corresponding ion. The PbFBr layer is terminated at the Hg surface by Br^- ions, which, contrary to F^-, are known to adsorb specifically on Hg (35). The model's fit parameters were the PbFBr surface coverage θ, a single width σ_L of the surface-normal ion distribution, common for all layers, a scale factor f accounting for a possible change in the layer's effective c, and the Br^-–Hg spacing d_{Hg-Br^-} shown in Fig. 2*A*. The gap between the outer Br^- ions and the error function describing the bulk electrolytes' termination (Fig. 2*A*) was found to be fit-insensitive and was therefore fixed at 3 Å, as found in our earlier measurements (16). The Hg layering parameters (d, $\overline{\sigma}$, σ_T) were also fitted. The partial Hg layer, required to model $R(q_z)$ at $\Phi = -0.90$ V, was found to be unnecessary here for a good fit, and was therefore excluded. Because the adlayer parameters were fixed at their bulk values (with the exception of f), this model has only seven fit parameters, comparable to models used in previous studies of Hg at solid and liquid interfaces (16, 23, 26, 28).

The model successfully reproduces the reflectivity curves at $\Phi = -0.60$ and -0.40 V, as shown in red and blue solid lines in Fig. 1*A*. The corresponding fit parameters are listed in Table 1. The fit values at the two potentials are found to be identical within their combined uncertainties.

Extensive attempts to describe the data by alternative models, assuming a PbFBr-like adlayer structure with a thickness of less than a full unit cell or consisting of single or double layers of the other compounds such as $PbBr_2$ and PbF_2, were unsuccessful (see Figs. S2–S4 and Tables S1–S3 for details on these models).

The electron density profiles corresponding to the best fits shown in Fig. 1*A* are displayed along with the chosen model in Fig. 2. They are dominated by the strongly scattering metal species, the two Pb layers and the Hg surface layering (marked by the dashed vertical lines in Fig. 2 *A* and *B*). The fit results in Table 1 show that the PbFBr adlayer leaves the Hg surface structure intact, except for reducing the interfacial roughness to $\sigma_T = 0.74 \pm 0.02$ Å. This behavior differs significantly from the very recent results of Duval et al., where the electrolytes' ions were found to strongly affect the Hg layering at the interface (17). The difference may arise from the 100-fold higher electrolyte concentrations used by Duval et al. The $f = 1$ (with an uncertainty of 3%) obtained indicates that the positions of the individual atomic layer within the adlayer remain unchanged from those in the 3D PbFBr unit cell. This supports strongly the presence of a $\vec{c}$-axis-oriented, crystalline PbFBr layer on the Hg surface, inferred above. $d_{Hg-Br^-} = 3.16 \pm 0.10$ Å is significantly larger than the value of 2.4 ± 0.3 Å found for close-packed Br^- layers on Au(111) (36). Although the difference is partially due to the smaller Au radius, a different adlayer–metal interaction, e.g., a less covalent metal–halide bond, may also be indicated. For all samples the surface coverage by the adlayer is remarkably high, with fit results of $\theta = 89 - 97\%$. Differences in full coverage may be due to the presence of larger 3D crystallites occupying the residual part of the surface.

Table 1. Structural parameters corresponding to the best fits of the data to the models described in the text

Phase	Parameter	−0.90 V	−0.60 V	−0.40 V
Hg	d [Å]	2.74 ± 0.05	2.72 ± 0.03	2.72 ± 0.03
	$\overline{\sigma}$ [Å]	0.44 ± 0.05	0.46 ± 0.05	0.46 ± 0.05
	σ_T [Å]	1.03 ± 0.02	0.74 ± 0.02	0.75 ± 0.02
PbFBr	θ		0.97 ± 0.10	0.89 ± 0.08
	σ_L [Å]		0.75 ± 0.03	0.73 ± 0.04
	f		1.00 ± 0.03	1.01 ± 0.03
	d_{Hg-Br^-} [Å]		3.16 ± 0.10	3.17 ± 0.06

Finally, we note that in close agreement with the Hg interfacial roughness σ_T, an out-of-plane distribution width of $\sigma_L = 0.74 \pm 0.04$ Å was determined for the atomic layers in the PbFBr adlayer. These σ_L and σ_T are substantially lower than σ_T at –0.90 V, enhancing the maxima of the $R(q_z)$ modulations for $\Phi > -0.60$ V well over the reflectivities at the same q_z positions for $\Phi < -0.60$ V. The decrease in roughness is contrary to expectations, because thermodynamically, interfacial adsorption of a foreign species occurs when the species reduces the surface energy γ, and hence increases $\sigma \sim 1/\gamma$ (37). The decrease in σ found here resembles observations for the liquid/vapor interfaces of Au–Si liquid eutectic (38) and of water-supported highly compressed Langmuir films (39). In both of these systems the liquid bulk is covered by a 2D solid, the nonzero bending rigidity of which quenches short-wavelength CWs. The reduced CWs' spectral range reduces σ and thus enhances $R(q_z)$. The upper wave-vector cutoff q_{max} required for our observed reduction in σ (neglecting the small Φ-induced change in γ) is $q_{max} = 0.1$ Å^{-1}. This cutoff corresponds to a bending rigidity of 100 kT, similar to that found for the solid surface bilayer on the liquid Au–Si eutectic (38). These similarities support the conclusion that the PbFBr adlayer is a 2D solid. A direct verification of this conclusion by X-ray diffuse scattering measurements, as done for Au–Si (38), is prohibited in our system by the high background scattering from the interface-overlying bulk electrolyte.

Discussion

The results presented above indicate two different regimes in the structure and electrochemical behavior of the interface. At $\Phi < \Phi_{rp}$ an amalgamation of Pb into Hg occurs, which, however, causes no observable change in the interface structure from that of a pure Hg interface. At $\Phi > \Phi_{rp}$ the Pb deamalgamation from Hg is accompanied by the formation of a full-surface–coverage, single-unit-cell–thick PbFBr adlayer, coexisting with a very low coverage of 3D PbFBr crystallites. The crystallites' c axis is coinciding with the q_z-parallel, $\vec{c}$ axis of the precursor adlayer, implying their quasiepitaxial growth at this liquid–liquid interface. The PbFBr adlayer and 3D crystalline phase form in the potential regime positive of Φ_{rp}. Upon decreasing the potential below Φ_{rp}, the Bragg peaks disappear and the $R(q_z)$ curve of the clean Hg surface is regained without any noticeable changes.

At present the nucleation and growth kinetics of the adlayer and crystallites have not been elucidated. However, a time-dependent growth behavior with an initial layer of well-defined thickness and a subsequent transition to 3D growth is observed (Fig. S5). This process resembles the Stranski–Krastanov growth found in many heteroepitaxial deposition processes at solid surfaces (40, 41). Stranski–Krastanov growth is commonly rationalized by the gradual buildup of stress in the deposited film, caused by the lattice mismatch of the deposit and the substrate. Although the liquid Hg surface exhibits lateral short-range order, which potentially couples elastically with the adlayer, this effect should be much smaller than for epitaxial growth on rigid solid substrates. Thus, conventional Stranski–Krastanov growth is not applicable for our case of a liquid substrate.

We propose therefore an alternative mechanism based on short-range chemical and electrostatic interactions of the adlayer with the Hg surface. For $\Phi > \Phi_{rp}$ and our Br^- concentration, Br^- is known to specifically adsorb onto the Hg surface, yielding at $\Phi = -0.60$ V a surface excess of $\Gamma_{Br^-} \approx 1.7 \times 10^{-10}$ mol cm^{-2}

or $\approx 4.4 \times 10^{14}$ Br^- ions per cm^2 (35). This is already $\approx 80\%$ of the Br^- layer density of crystalline PbFBr. As common in specific adsorption, Pb^{2+} counter ions, released from the Hg bulk, will accumulate on top of this adsorbed Br^- layer and form the next ion layer of the PbFBr compound.

The surprising formation of a full unit cell of five atomic layers of different ionic composition, rather than one double layer only, can be explained by electrostatics, which require subsequent adsorption of oppositely charged ionic layers until full charge neutrality is achieved upon reaching a full unit cell structure, minimizing the surface energy. This adsorption is driven by the charge density per unit area of the Pb^{2+} and F^- layers being twice that of the Br^- layer. The formation of simpler compounds consisting of fewer layers, e.g., $PbBr_2$, is energetically less favorable due to the lower Gibbs enthalpy of PbFBr (42). For similar electrostatic reasons, the actual adlayer formation process most likely proceeds via nucleation and subsequent 2D growth of PbFBr adlayer islands on the Br^--covered Hg surface.

The combined mechanism proposed above explains the well-defined thickness as well as the $\vec{c}$-axis orientation of the adlayer film. The formation of such well-defined ultrathin salt-like compound films is a well-established phenomenon on solid metal electrode surfaces (43). For example, Tl^{2+} and Br^- ions have been shown to form well-ordered $TlBr_2$ and TlBr surface compounds on Au(111) electrodes (44). Similar to our Φ-range, these adlayers were formed at potentials a few hundred millivolts positive of the potential of zero charge, where coadsorption of both anionic and cationic species is favored. However, a well-defined, uniform adlayer of the complexity found here, comprising five atomic layers and three ionic species, has not been reported to date.

Although the chemical interactions between Br^- and the Hg surface and the excess charge located at the interface can stabilize the PbFBr adlayer, they will rapidly decrease at larger distances from the surface and will not promote the growth of thicker adlayers. Growth of the second and further PbFBr unit cells requires nucleation on the Br^--terminated outer surface of the adlayer. This will be hindered by the weak (van der Waals) interactions between the Br^- layers of PbFBr, and by kinetic barriers, e.g., the one associated with the stripping of the outer Br^- layer's hydration layer. Nevertheless, the precursor adlayer apparently still can serve as a template for the subsequent growth of crystallites, which presumably form pseudomorphically on some of the ordered domains of the quasi-2D film.

In a sense, the adlayer formation process may be viewed as a controlled precipitation, where the electrochemical deamalgamation reaction increases the Pb^{2+} concentration near the surface beyond the PbFBr solubility product, promoting formation of the solid adlayer. Vice versa, the decrease in concentration during amalgamation leads to fast PbFBr dissolution, prohibiting adlayer formation. Previous studies of deposition at liquid–liquid interfaces resolved only the structure of films that were tens of nanometers thick, as well as of 2D assemblies of nanoparticles, albeit usually without a well-defined crystalline orientation (1–4, 6, 45). However, the observation of the very early stage of the deposition, showing a subnanometer-thick, structurally well-defined precursor film that governs the subsequent growth of 3D crystallites is unique. Similar adsorption phenomena and associated epitaxial effects are expected for growth at other fluid interfaces, especially for crystal growth on strongly correlated high surface energy liquids, such as liquid metals, melts, and ionic liquids. In particular, the mechanism proposed here for PbFBr growth should also be relevant for other ionic compounds such as oxides (4), halides (18), or sulfides (4–6), where indeed indirect evidence of quasiepitaxial effects have been observed. This may allow the controlled growth of a multitude of interesting compounds, e.g., II–VI semiconductors. Overall, this study provides insight into an interesting route for solvated ions self-assembly into 2D and 3D crystalline structure, 3and on ways for its electrochemical control. Time-dependent X-ray measurements may shed further light on the time evolution and kinetics of the nucleation and growth of both the adlayer and the 3D crystallites. Measurements at Φ closer to Φ_{rp} may also reveal variations in the evolution and the structure, and provide further insight on the early stages of crystal nucleation and growth.

Materials and Methods

The experiments were performed at an X-ray energy of 25.05 keV at the liquid interfaces scattering apparatus (LISA) diffractometer (46) of the high-resolution diffraction beamline P08 of the PETRA III synchrotron at Deutsches Elektronensynchrotron (DESY) (47) and at beamline ID-9, Advanced Photon Source (22.12 keV). A linear Mythen (Dectris) detector was used, comprising 1,280 independent detector pixels, each 50 μm high.

A dedicated electrochemical cell for X-ray scattering studies (16) was used, in which the potential of the 4-cm–diameter Hg pool was controlled relative to a Hg/Hg_2SO_4 reference electrode (Schott). The Hg sample was first immersed and characterized by cyclic voltammetry and XRR in neat 0.01 M NaF solution to ensure a clean, well-defined interface. Subsequently, NaBr and $PbBr_2$ solutions were added to the NaF base solution under high-purity nitrogen atmosphere until concentrations of $\sim$0.01 M NaBr and $\sim$0.25 mM $PbBr_2$ were reached. These solutions were added under a constant potential of −0.85 V. XRR and voltammetry were started within minutes of reaching the required concentration.

The master equation relating the reflectivity curve $R(q_z)$ and the interface-normal electron density profile $\rho_e(z)$ are given in refs. 20–22. The mathematical expression of the DC $\rho_e(z)$ model used to fit the $R(q_z)$ curves is given in refs. 16, 17, 23, 28.

ACKNOWLEDGMENTS. We thank the beamline staff of P08 at PETRA III and Dr. I. Kuzmenko and the staff of ID-9 at the Advanced Photon Source for their support. This work is supported by the Bundesministerium fuer Bildung und Forschung (BMBF) (Project 05KS10FK2), the United States–Israel Binational Science Foundation, and by the US Department of Energy, Basic Energy Sciences, Materials Sciences and Engineering Division, supported under Contract DE-AC02-98CH10886.

1. Krishnaswamy R, Sood AK (2010) Growth, self-assembly and dynamics of nano-scale films at fluid interfaces. *J Mater Chem* 20:3539–3552.
2. Rao CNR, Kalyanikutty KP (2008) The liquid-liquid interface as a medium to generate nanocrystalline films of inorganic materials. *Acc Chem Res* 41(4):489–499.
3. Mlondo SN, Thomas PJ, O'Brien P (2009) Facile deposition of nanodimensional ceria particles and their assembly into conformal films at liquid-liquid interface with a phase transfer catalyst. *J Am Chem Soc* 131(17):6072–6073.
4. Gautam UK, Ghosh M, Rao CNR (2004) Template-free chemical route to ultrathin single-crystalline films of CuS and CuO employing the liquid-liquid interface. *Langmuir* 20(25):10775–10778.
5. Fan D, Thomas PJ, O'Brien P (2008) Pyramidal lead sulfide crystallites with high energy {113} facets. *J Am Chem Soc* 130(33):10892–10894.
6. Zhuang Z, Peng Q, Zhang B, Li Y (2008) Controllable synthesis of Cu_2S nanocrystals and their assembly into a superlattice. *J Am Chem Soc* 130(32):10482–10483.
7. Nuraje N, Su K, Yang NL, Matsui H (2008) Liquid/Liquid interfacial polymerization to grow single crystalline nanoneedles of various conducting polymers. *ACS Nano* 2(3):502–506.
8. Dryfe RAW, Simm AO, Kralj B (2003) Electroless deposition of palladium at bare and templated liquid/liquid interfaces. *J Am Chem Soc* 125(43):13014–13015.
9. Platt M, Dryfe RAW, Roberts EPL (2003) Electrodeposition of palladium nanoparticles at the liquid-liquid interface using porous alumina templates. *Electrochim Acta* 48:3037–3046.
10. Platt M, Dryfe RAW, Roberts EPL (2003) Structural and electrochemical characterisation of Pt and Pd nanoparticles electrodeposited at the liquid/liquid interface. *Electrochim Acta* 49:3937–3945.
11. Carim AI, Collins SM, Foley JM, Maldonado S (2011) Benchtop electrochemical liquid-liquid-solid growth of nanostructured crystalline germanium. *J Am Chem Soc* 133(34):13292–13295.
12. Dryfe RAW (2006) Modifying the liquid/liquid interface: Pores, particles and deposition. *Phys Chem Chem Phys* 8(16):1869–1883.
13. Cantin S, Pignat J, Daillant J, Perrot F, Konovalov O (2010) Grazing incidence X-ray diffraction determination of the structure of two-dimensional organic-inorganic crystals at the water surface. *Soft Matter* 6:1923–1932.
14. Sanyal MK, et al. (2008) Formation and ordering gold nanoparticles at the toluene-water interface. *J Phys Chem C* 112:1739–1743.

15. Bera MK, et al. (2010) Small-angle x-ray scattering study of the aggregation of gold nanoparticles during formation at the toluene-water interface. *Phys Rev B* 81:115415.
16. Elsen A, et al. (2010) Surface layering at the mercury-electrolyte interface. *Phys Rev Lett* 104(10):105501.
17. Duval JFL, et al. (2012) X-ray reflectivity at polarized liquid-Hg-aqueous-electrolyte interface: Challenging macroscopic approaches for ion-specificity issues. *Phys Rev Lett* 108(20):206102.
18. Herman HB, McNeely RL, Surana P, Elliott CM, Murray RW (1974) Surface solubility and reaction inhibition in lead bromide and iodide adsorbed on mercury electrodes. *Anal Chem* 46:1258–1265.
19. Lovrić M, Komorsky-Lovrić S (1995) Adsorption of $PbBr_2$ complex on mercury electrodes. *Langmuir* 11:1784–1790.
20. Deutsch M, Ocko BM (1998) in Encyclopedia of Applied Physics, vol 23, ed Trigg GL (VCH, New York), pp 479.
21. Als-Nielsen J, McMorrow D (2001) *Elements of Modern X-Ray Physics* (Wiley, New York).
22. Pershan PS, Schlossman ML (2012) *Liquid Surfaces and Interfaces: Synchrotron X-Ray Methods* (Cambridge Univ Press, Cambridge, UK).
23. Magnussen OM, et al. (1995) X-ray reflectivity measurements of surface layering in liquid mercury. *Phys Rev Lett* 74(22):4444–4447.
24. Tamam L, Ocko BM, Reichert H, Deutsch M (2011) Checkerboard self-patterning of an ionic liquid film on mercury. *Phys Rev Lett* 106(19):197801.
25. Tamam L, et al. (2011) Modification of deeply buried hydrophobic interfaces by ionic surfactants. *Proc Natl Acad Sci USA* 108(14):5522–5525.
26. Tamam L, et al. (2010) Atomic-scale structure of a liquid metal-insulator interface. *J Phys Chem Lett* 1:1041–1045.
27. Ocko BM, et al. (1997) Surface freezing in chain molecules: Normal alkanes. *Phys Rev E Stat Phys Plasmas Fluids Relat Interdiscip Topics* 55:3164–3182.
28. DiMasi E, Tostmann H, Ocko BM, Pershan PS, Deutsch M (1995) X-ray reflectivity study of temperature-dependent surface layering in liquid Hg. *Phys Rev B* 58(20): R13419–R13422.
29. Ocko BM, Wu XZ, Sirota EB, Sinha SK, Deutsch M (1994) X-ray reflectivity study of thermal capillary waves on liquid surfaces. *Phys Rev Lett* 72(2):242–245.
30. Pershan PS (2009) X-ray scattering from liquid surfaces: Effect of resolution. *J Phys Chem B* 113(12):3639–3646.
31. Downs RT, Hall-Wallace M (2003) The American Mineralogist Crystal Structure Database. *Am Mineral* 88:247–250.
32. Gražulis S, et al. (2009) Crystallography Open Database - an open-access collection of crystal structures. *J Appl Cryst* 42(Pt 4):726–729.
33. Gražulis S, et al. (2012) Crystallography Open Database (COD): An open-access collection of crystal structures and platform for world-wide collaboration. *Nucleic Acids Res* 40:D420–D427.
34. Nieuwenkamp W, Bijvoet JM (1932) Die Kristallstruktur von Bleifluobromid. *Z Kristallogr* 82:157–160.
35. Lawrence J, Parsons R, Payne R (1968) Adsorption of halides at the mercury-water interface. *Electroanal Chem Interfacial Electrochem* 16:193–206.
36. Wang J, Ocko BM, Davenport AJ, Isaacs HS (1992) In situ x-ray-diffraction and -reflectivity studies of the Au(111)/electrolyte interface: Reconstruction and anion adsorption. *Phys Rev B Condens Matter* 46(16):10321–10338.
37. Defay R, Prigogine I, Bellemans A, Everett DH (1966) *Surface Tension and Adsorption* (Wiley, New York).
38. Mechler S, et al. (2010) Self-consistent interpretation of the 2D structure of the liquid $Au_{82}Si_{18}$ surface: Bending rigidity and the Debye-Waller effect. *Phys Rev Lett* 105(18): 186101.
39. Daillant J, Bosio L, Benattar JJ, Meunier J (1989) Capillary waves and bending elasticity of monolayers on water studies by X-ray reflectivity as a function of surface pressure. *Europhys Lett* 8(5):453–458.
40. Stranski IN, Krastanov L (1937) Zur Theorie der orientierten Ausscheidung von Ionenkristallen aufeinander. Sitzungsberichte der kaiserlichen Akademie der Wissenschaften in Wien. *Math-Naturwiss Classe, Abt IIB Chemie* 146:797–810.
41. Baskaran A, Smereka P (2012) Mechanisms of Stranski-Krastanov growth. *J Appl Phys* 111:044321.
42. Wagman DD, et al. (1982) The NBS tables of chemical and thermodynamic properties: Selected values for inorganic C1 and C2 organic substances in SI units. *J Phys Chem Ref Data* 11:1–392.
43. Magnussen OM (2002) Ordered anion adlayers on metal electrode surfaces. *Chem Rev* 102(3):679–725.
44. Wang JX, Robinson IK, Adzic RR (1998) Formation of well-ordered surface compounds by coadsorption of thallium and bromide on the Au(111) electrode surface. *Surf Sci* 412/413:374–383.
45. Lin Y, Skaff H, Emrick T, Dinsmore AD, Russell TP (2003) Nanoparticle assembly and transport at liquid-liquid interfaces. *Science* 299(5604):226–229.
46. Murphy BM, et al. (2010) A new diffractometer for studies of liquid-liquid interfaces. *AIP Conf Proc* 1234:155–158.
47. Seeck OH, et al. (2012) The high-resolution diffraction beamline P08 at PETRA III. *J Synchrotron Radiat* 19:30–38.